Estimate of the D/H ratio in the Martian upper atmosphere from the low spectral resolution mode of MAVEN/IUVS

Jean-Yves Chaufray, M. Mayyasi, M. Chaffin, J. Deighan, D. Bhattacharyya, J. Clarke, S. Jain, N. Schneider, B. Jakosky

Estimate of the D/H ratio in the Martian upper atmosphere from the low spectral resolution mode of MAVEN/IUVS

J-Y. Chaufray[1], M. Mayyasi[2], M. Chaffin[3], J. Deighan[3], D. Bhattacharyya[4], J. Clarke[2], S. Jain[3], N. Schneider[3], and B. Jakosky[3]

[1]LATMOS-IPSL, CNRS, UVSQ Université Paris-Saclay, Sorbonne Université, Guyancourt, France

[2] Center for Space Physics, Boston University, Boston, Massachusetts, USA

[3] LASP, University of Colorado Boulder, Boulder, Colorado, USA

[4]Department of Electrical and Computer Engineering, University of Illinois at Urbana-Champaign

Abstract

Recent MAVEN observations have shown unexpectedly large deuterium Lyman-α emissions near the Martian southern summer solstice. The deuterium Lyman-α brightness can reach ~ 10% of the hydrogen Lyman-α brightness below 200 km. In this paper, we propose a method to estimate the D/H ratio in the Martian upper atmosphere through analysis of the Lyman-α vertical profiles without the ability to spectrally separate the two atomic emission lines. Lyman-α vertical profiles measured by MAVEN/IUVS at four periods are analyzed. During southern summer, the derived D/H ratios at 200 km are larger than the HDO/H_2O ratio measured in the lower atmosphere, yet the extrapolated D/H ratio from 200 to 80 km agrees with the HDO/H_2O ratio. This larger D/H ratio at higher altitude is attributed to the more efficient escape of hydrogen atoms compared to deuterium atoms. The method we describe accounts for uncertainties related to constraining the temperature and density profiles of H and D in the lower thermosphere. Because spectrally-resolved D and H Lyman-α measurements are not always available, this method provides a way to estimate D/H variations in their absence. This method will be useful for analysis of relevant datasets from past and future Mars missions.

This article has been accepted for publication and undergone full peer review but has not been through the copyediting, typesetting, pagination and proofreading process, which may lead to differences between this version and the Version of Record. Please cite this article as doi: 10.1029/2020JE006814.

Plain Language Summary

Water vapor in the Martian atmosphere is enriched in deuterium, compared to the atmosphere and oceans of Earth. This enrichment is caused by the preferential escape of atomic hydrogen over its deuterium isotope, as integrated over time, due to its lower mass. Therefore, measuring the D/H ratio and understanding its spatial and temporal variation is important for estimating the evolution of water escape from Mars over time. In this study, we use models to estimate the D/H ratio at 80 and 200 km from low resolution Lyman-α limb profiles measured by the Imaging Ultraviolet Spectrograph (IUVS) aboard the Mars Atmosphere and Volatile EvolutioN (MAVEN). During the southern summer season at Mars, the derived D/H ratio profiles, extrapolated down to 80 km, agree with the HDO/H_2O ratio measured by other instruments. However, at 200 km, the derived H/D ratios are larger than in the lower atmosphere due to the more efficient escape of lighter hydrogen atoms compared to deuterium atoms. The main sources of uncertainties in the D/H ratio derivation are also presented.

1. Introduction

Estimating the water escape rate throughout Mars' history depends strongly on the water reservoirs available to exchange with the atmosphere, and the timescale for that exchange. The D/H ratio in a planetary atmosphere is a key parameter for diagnosing water loss from a planet. Hydrogen and deuterium atoms can escape through a variety of processes that need to be constrained to accurately estimate present and past water loss rates (e.g. Cangi et al. 2020). On Mars, the globally averaged D/H ratio is five times larger than that measured in the terrestrial oceans (Owen et al. 1988,

Encrenaz et al., 2018, Vandaele et al. 2019). The deuterium enrichment on Mars results from the long-term preferential escape of lighter hydrogen atoms over heavier deuterium atoms. Systematic measurement of the D/H ratio in the Martian upper atmosphere is one of the main goals of the Imaging Ultraviolet Spectrograph (IUVS) aboard the Mars Atmosphere and Volatile EvolutioN (MAVEN).

The IUVS instrument has Far-UV (110-190 nm) and Mid-UV (180-340 nm) channels, with spectral resolutions of 0.6 and 1.2 nm, respectively. The Far-UV channel includes an echelle grating, with a spectral resolution of 80 mA, that can resolve the deuterium and hydrogen Lyman-α emissions (McClintock et al. 2015). In this study, we will refer to the Lyman-α observations obtained by the Far-UV channel as "low-resolution" and those obtained with the echelle grating as "high-resolution".

Early in the MAVEN mission when Mars was close to perihelion, the deuterium Lyman-αbrightness, observed with the IUVS high-resolution mode was ~ 1 kR (Clarke et al. 2017, Mayyasi et al. 2017). This brightness was much larger than the first two Martian deuterium detections from Earth, ~ 20-50 R while Mars was near aphelion (Bertaux et al., 1993, Krasnopolsky et al. 1998). Subsequent MAVEN observations showed consistently low deuterium emission brightnesses near aphelion (Mayyasi et al., 2017). Analysis of D and H high resolution profiles, obtained below 300 km, showed significant seasonal variations of deuterium abundance at 200 km (Mayyasi et al. 2019, Bhattacharyya et al. 2020). D densities were found to increase from 1000±200 cm^{-3} near Ls=220°, to a peak density of 3000±1000 near Ls=290°, then to decrease once more, down to 1600±1000 cm^{-3} toward the end of the dusty season (Ls=330°). Chaffin et al. (2018) fit several low-resolution profiles obtained above 500 km to estimate the deuterium density at 200 km. The fitted values were

1900±800 cm^{-3} at Ls=200° and 4600±1000 cm^{-3} at Ls = 260°, substantially larger than the densities estimated using high-spectral resolution data.

Light species, such as hydrogen (H) and helium (He) are expected to be more abundant at night reaching peak abundance in the early morning during the southern summer season (Chaufray et al. 2015a, 2018, Elrod et al. 2017). It is likely that a global enhancement of deuterium (D) will also occur on the nightside and that D will reach its maximum abundance in the early morning. D emissions are optically thin at Lyman-α thus the volume emission rate is the product of the excitation frequency (g-factor) and the local D atom number density. The excitation frequency is almost uniform except in the nightside shadow region (solar zenith angle > 105° at 110 km) where no excitation can occur. The optically thin D Lyman-α emission will be brighter during limb viewing near the terminator (outside the shadow) than at lower solar zenith angles (SZA) because the density and path length is at its peak and the excitation frequency not undimnished. For an optically thick emission like the H Lyman-α, the excitation frequency decreases with increasing SZA due to the scattering of the solar photons along their propagation path in the atmosphere. The volume emisson rate for H Lyman-α is therefore also expected to decrease with higher SZA (e.g. Chaffin et al. 2015). Due to these differences in D and H volume emission rates, the ratio of the deuterium brightness and the hydrogen brightness should be largest for limb-viewing near the morning terminator.

In early 2015, it was found that IUVS low-resolution observations made near the morning terminator during southern summer season (solar longitude, Ls = 270°) were not reproducible with models that included only emission from the thermal H population (Chaffin et al. 2015). During this time, there were no simultaneous measurements made with IUVS high-resolution mode that could be used to constrain the additional D Lyman-α emissions. In this study, we further investigate

the possible contribution of the deuterium Lyman-α emission to low-resolution observations in order to explain the observed vertical profile of the brightness, including observations below 500 km. To validate our method, we also consider other periods where the deuterium emission has been detected with high-resolution observations. In section 2, we describe a specific set of low-resolution observations that were analyzed along with an overlapping subset of high-resolution observations that were used to validate our approach. Models used to interpret the observations are presented in section 3, validation results are presented in section 4, and effects of systematic uncertainties are presented in section 5. The deuterium and hydrogen densities, derived for four chosen periods, are presented and discussed in section 6 followed by conclusion in section 7.

2. Observations

MAVEN-IUVS observations of the Martian limb are used for this study (McClintock et al. 2015). The instrument line-of-sight is in the orbital plane of the spacecraft, with the slit parallel to the normal of the orbital plane (Chaffin et al. 2015, Deighan et al. 2015, Chaufray et al. 2020). Observations with a tangent altitude spanning the surface to ~250 – 400 km, obtained when MAVEN was on the outbound portion of its orbit, are referred to as “outlimb”, in the Planetary Data System (PDS) archives. Observations with tangent altitude spanning ~350 – 3200 km, also obtained when MAVEN was on the outbound portion of its orbit, are referred to as “outcorona” in the PDS. Limb-pointed observations are used (rather than disk-pointed) since they show brightness profiles with altitude that are needed to constrain the deuterium density from the low-resolution mode. Four periods are usedto study deuterium brightness with the low-resolution mode.

The two first periods correspond to southern summer of Martian Years 33 and 34, respectively, where the deuterium emission was detected at the limb with thehigh-resolution mode. These two

observation periods are therefore used to validate the retrieval since separate D and H Lyman-α vertical profiles are available with similar observing geometry for the low-resolution mode.

The third observation period corresponds to a time when no deuterium was detected above the noise level of the high-resolution mode. The deuterium brightness at the limb is therefore likely to be less than the 3-□ detection threshold of the IUVS detector, ~300 R (Mayyasi et al., 2019). This period is used to test that the retrieval method confirms no deuterium is needed to reasonably match these observations.

The fourth observation period corresponds to southern summer of Martian Year 32. During this period, no contemporaneous high-resolution mode observations were taken while pointed at the limb, however there were disk-pointed observations (Clarke et al. 2017). The observations from this period, near the morning terminator, were examined by Chaffin et al. (2015), and were found to be irreproducible by a model that used a single-hydrogen population.

The MAVEN-IUVS observation geometry from each period is summarized in Table 1.

Orbit #

Period 2: near southern solstice MY 34 with simultaneous high-resolution observations 7780

Figure 1: Examples of vertical profiles of Lyman-α brightness obtained during the four periods. Orbit #4359 from period 1 (blue), orbit #7788 from period 2 (green), orbit #1570 from period 3(pink) and orbit #786 from period 4 (black) are shown. The integration time used for the "outlimb" observations (below ~350-400 km) is shorter than the integration time used for the "outcorona" (above ~350 – 400 km) leading to a noiser profile but with finer spatial resolution. For orbit #4359 only one outlimb of the available four is diplayed, while for orbit #7788, only the first (SZA = 79°, left green curve) and sixth outlimb (SZA= 54°, right green curve) are displayed for clarity.

The integration time for the "outlimb" segment (below ~350 – 400 km) was shorter than the integration time for the "outcorona" segment (above ~350-400 km) in order to obtain better spatial sampling closer to the planet (~5 km sampling for the limb scan and ~35 km for the coronal scan). Therefore, the data is noisier near the limb. A bright limb is observed for orbits #4359 and #7788, and to a lesser extent in orbit #786 near 120 km mostly due to proton aurorae (Hughes et al. 2019).

As already mentioned, during the two first studied periods, four and six limb scans were obtained for each orbit, respectively. Example brightness profiles from period 1for orbit #4351 , are shown in Figure 2. Variations from one limb scan to another are small and attributed to various solar zenith

angles of 80°, 84°, 87° and 90° (Fig. 2, left panel). Data obtained with the FUV 1024x1024 pixel detector is binned differently for different observation modes. For the data used in this study, data were consistently binned into seven spatial bins, with each bin as the sum of 115 physical pixels of the detector along the slit. The differences in the brightness between spatial bins is small and mostly due to the non-uniform sensitivity of the detector (Fig. 2, right panel). Only spatial bins 1-5 are used in this work due to their higher sensitivity. For the observations of the second period, the variability from one limb scan to another is larger (Fig. 1) due to the larger variations in SZA (Table 1) as expected for the H Lyman-α optically thick emission (Clarke et al 2014, Chaffin et al. 2015).

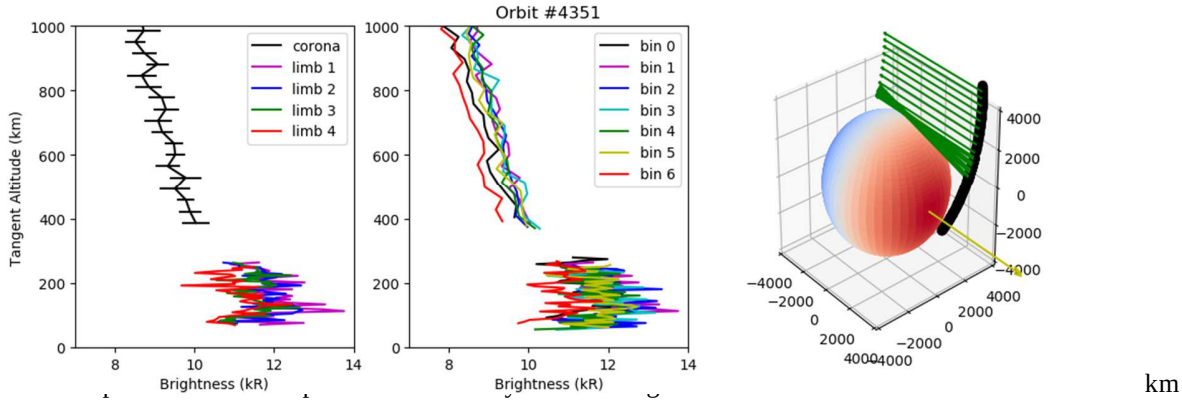

for spatial bin 1. The four limb scans obtained at SZA = 80° (limb 1), 84° (limb 2), 87° (limb 3) and 90° (limb 4) and the coronal scan (SZA = 90°) are shown. The uncertainty associated with each measurement is ~ 600 R for the limb scans (not displayed for clarity) and ~ 300 R for the coronal scan. Middle panel: Lyman-α brightness profiles of orbit 4351 observed on 26 December 2016 for the first limb scan (tangent altitude between 0 and 250 km) and for the coronal scan (tangent altitude greater than 350 km) for each of the 7 spatial bins. Right panel: Geometry of the observation during orbit 4351 in the Mars Sun Orbit (MSO) frame. All axis are in km. The Martian surface is red at the dayside and blue at the nightside. MAVEN is moving from the bottom to the

top and its position is represented by the black solid line. The lines of sight of IUVS during the four limb scans (near the Martian surface) and the coronal scan are represented in green. The sun direction is shown by the yellow arrow (X axis).

Figures 3 and 4 show the average profile for the first two periods, respectively, derived from all observations using the low-resolution and high-resolution modes. The vertical sampling of the low-resolution mode for one individual limb scan is 5 km. For the low-resolution mode, the average profile was obtained by binning the data with a vertical resolution of 40 km below 50 km, 20 km between 50 - 80 km altitude, 5 or 10 km between 80-160 km altitude, and 20 km above 160 km altitude. For the high-resolution data, the vertical binning was between 30 -40 km for period 1, and between 10 -50 km for period 2. Only observations where the SZA was between 80° – 90° and 50 – 60° were used for period 1 and 2, respectively.

Figure 3. Comparison between the average Lyman-α brightness profile obtained with the low-resolution mode, labeled "FUV" (blue), obtained from the subset of observations (SZA between

80 -90°) during period 1, and the high-resolution high-resolution mode (able to spectrally separate D and H Lyman-α lines) for a similar geometry. The error bars correspond to the standard deviation of all observations done in each altitude range, and therefore include both real variability and data noise. For the high-resolution mode, the statistic is limited to 2-6 observations in each altitude bin, and so the standard deviation is not statistically significant. Therefore, we compute the standard deviation from all high-resolution data between 0 to 300 km and assume the same value at all altitudes for both D and H. The two horizontal black lines on the right indicate the approximate altitudes, where the vertical and limb view CO_2 optical depth is unity.

Figure 4. Same as Figure 3 but for period 2. For this period, the number of observations inside each altitude bin for the high-resolution mode varies between 3 and 29 and therefore, the standard deviation is derived separately for each altitude bin. The two horizontal black lines on the right indicate the approximate altitudes, where the vertical and limb view CO_2 optical depth is unity

The differences in D+H brightness between the low-resolution and the high-resolution modes at these altitude ranges are less than 10% and within the range of the uncertainties of each channel (Chaffin et al., 2015; Mayyasi et al., 2017); this agreement is sufficient. The increase of the H Lyman-α emission from 100 km to 150 km is mostly due to the contribution of the interplanetary

medium (on the order of 100s R), and the planetary contribution of the hydrogen past the tangent line which is fully absorbed by the CO_2 below ~ 100 km and not absorbed above 150 km.

The bright limb near 120 km is evident in the average profiles derived from the low-resolution mode for the two periods. Limb brightening is not expected for the hydrogen emission because it is optically thick, but with moderate thickness (τ ~10) the contribution of the spectral wings is not important. Lyman-α limb brightening can be produced by proton aurorae (Deighan et al. 2018, Hughes et al. 2019), and the deuterium bright limb observed with the high-resolution mode is present but rather weak (Fig. 3, Fig 4.). The bright limb is likely due to proton aurora, which is not accounted for in our models. Therefore, in this study, we only fit the data above 160 km where auroral emission should be 10 to 20 times less than the brightness at 120 km (Gérard et al. 2019).

3. Models

3.1 Density models

In order to separate the deuterium signal from hydrogen in the low-resolution mode we use a forward approach, simulating the expected brightness for different hydrogen density profiles and looking for the profile which best matches the data. Contrary to Chaffin et al. (2018), we use a simple fit method with only two free parameters (density of hydrogen and density of deuterium at a reference altitude). Chaffin et al. (2018) have shown that the study of a large set of observations with a more accurate method would require a prohibitive amount of computational time. Our goal is to show that useful information on the D/H ratio in the Martian upper atmosphere can be derived from the spectrally unresolved Lyman-α lines of D and H. The simple fit approach is therefore considered sufficient, and the effects of other unconstrained parameters are discussed in detail in

section 5. Improved estimates, using a larger set of free parameters could be performed in the future.

The model density profiles (from 80 km to 50,000 km) used to compute the brightness profiles are parametrized by the hydrogen and deuterium densities at the exobase and the temperature at the exobase (see Chaufray et al. 2008, appendix A). The temperature is chosen in a range close to the temperature derived from the MAVEN Neutral Gas and Ion Mass Spectrometer (NGIMS) measurements using the first eight MAVEN dip-deep campaigns (Stone et al. 2018). The deuterium and hydrogen densities at the exobase are the two free parameters. Sensitivity of variations in the exospheric temperature on the derived D/H ratio are presented in section 4.2.

Recently, it has been suggested that near southern summer, most of the atomic hydrogen in the upper atmosphere could come from water vapor dissociation in the Martian mesosphere/thermosphere (Chaffin et al. 2017, Stone et al. 2020). In this case the hydrogen density profile could be close to perfect mixing with CO_2 between 80 and 120 km (Krasnopolsky 2019, Chaufray et al. 2021). Therefore, we have performed a set of simulations, solving the diffusion equation as done by Chaufray et al. (2008) but without imposing a constant density below 120 km (case 1). In Chaufray et al. (2008), the hydrogen density profile was constant between 80 and 120 km to mimic the effects of the photochemical reactions (between H_2 and CO_2^+) on the density profiles. We performed another set of simulations with this assumption (case 2). The vertical profiles of the thermospheric temperature and the eddy diffusion coefficient are taken from Krasnopolsky (2002). Examples of H and D density profiles for an exospheric temperature of 180 K are shown in Figure 5 for the two cases considered. These two cases can be considered as lower and upper estimates of the density below 120 km. The real profile should be in-between (Krasnopolsky 2019).

Figure 6. Top: Examples of the modeled hydrogen and deuterium density from 50 km to 10,000 km. The temperature profile is also represented in black. Bottom: Model of the EMI ratio profile derived from the density profiles shown above.

The simulated vertical EMI ratio is displayed in Fig. 6. Below 140 km, the EMI ratio increases with altitude up to a peak at ~140 km. This increase is due to Jeans escape which reduces the scale height of the density profile (e.g. Chamberlain and Smith 1970) in the lower thermosphere where the molecular diffusion coefficient begins to fall due to collisions ($\propto p^{-1}$ where p is the diffusion pressure and n_a is atmospheric density). For H, this reduction in scale height increases the vertical velocity w in large, but its loss impacts the thermosphere at 150 K (the Jeans effusion velocity for H is ~ 1.93 km/s while it is 0.16 km/s for D). The diffusion equation that includes escape is given by:

The reduction of the hydrogen density scale height due to the escape rate (Eq. 3) explains the increase of the D/H ratio with altitude between 80 and 140 km by a factor 2 and 1.1 for cases 1 and 2, respectively.

At higher altitudes (above ~160 km), w(z) << u(z) and $m_{eff} \sim m_H$, so the decrease in the D/H ratio is expected and due to the larger scale height of H. Non-thermal escape of atomic deuterium, expected to be large at low solar minimum (Krasnopolsky 2002, Cangi et al. 2020), should increase the deuterium vertical velocity and then reduce its scale height below 140 km (Eq. 2). Therefore, the simulated D/H increase between 80 and 140 km in this model is an overestimate.

The density profiles above 200 km are computed using a Chamberlain model (Chamberlain 1963) up to 50,000 km. The full hydrogen and deuterium density profiles each depend on only two quantities, their density and temperature at the exobase.

3.2 Radiative transfer model

We use a Monte Carlo radiative transfer model to simulate the spectral volume emission rate of both H and D. This model has been validated with the matricial model of Chaufray et al. (2008) and was used to study the Venusian hydrogen corona (Chaufray et al. 2012, 2015b). This model considers the angle-dependent partial frequency redistribution and non-uniform temperature profiles. In all the simulations presented here, we use a version including only one thermal population, since non-thermal populations are negligible at the studied altitudes (Bhattacharyya et al. 2017). The hydrogen and deuterium spectral volume emission rates are simulated independently (the lines are separated by ~40 Doppler units at 200 K) and vary with altitude and solar zenith angle only.

The deuterium emission is optically thin; therefore, using a radiative transfer model should not be needed. However other effects such as partial absorption by CO_2 and the Martian shadow need to be considered to properly describe the volume emission rates at large SZA or low altitudes. Since these effects are included in the radiative transfer model that can simulate the volume emission rate for an optically thin or thick emission, we adapt it to simulate the deuterium Lyman-α emission.

The D and H brightnesses depend linearly on the flux near the center of the solar Lyman-α line. The integrated solar Lyman-α line is taken from the MAVEN Extreme Ultraviolet Monitor (EUVM) measurements, assuming all the solar flux between 121 and 122 nm is due to the solar Lyman-α line, and using the relation of Emerich et al. (2005) to relate integrated solar flux to the solar flux at the center of the line. We use the same value to calculate the hydrogen and deuterium excitation frequency. Observations of the solar Lyman-α spectral line by the Solar Ultraviolet Measurement of Emitted Radiation (SUMER) instrument on the Solar and Heliospheric Observatory (SOHO) show that the differences should be less than 20% (Lemaire et al. 2005). An increase or decrease of the simulated deuterium brightness by 20% will increase/decrease the total (hydrogen + deuterium) simulated brightness by less than 3%. The associated uncertainty is therefore considered to be negligible compared to other sources of uncertainty which arediscussed below.

The interplanetary background is assumed to be 500 R, a sensitivity study of this parameter is performed in section 5.

4. Validation of the method

To validate this method, we simulate hypothetical deuterium and hydrogen Lyman-α profiles assuming a hydrogen density of $2x10^5\,cm^{-3}$, deuterium density of $10^3\,cm^{-3}$, and a temperature of

200 K at the exobase with the geometric conditions of orbit #4370. A contribution of 500 R due to the interplanetary hydrogen is added above 110 km. A Gaussian noise of magnitude σ_I is added to the simulated profile which is then fitted using the same method for all observations. A sample simulated profile and corresponding best fit are displayed in Figure 6.

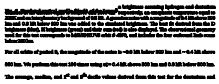

hydrogen densities at the exobase are given in Table 2. For this test the simulated D/H brightness ratio at the bright limb (without noise) is ~ 0.14.

Parameter

The exospheric temperature is a crucial parameter to derive the hydrogen density from a Lyman-α observation with forward models (Chaufray et al. 2008). Here we consider different values of the exospheric temperature to determine how the derived D/H ratio vary. The best fit obtained for orbit #4355 (first period), band 1 are displayed in Fig. 7 for T = 160K, T=180K, and T = 200K.

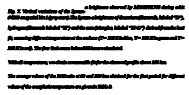

# T	nH (80)	nD (80)	D/H (80 km)	nH (200)	nD (200)	D/H (200 km)	$<\chi^2>$
160							

emissions may be very weak near the terminator, thereby requiring observations from in-situ instruments or models. In the following sections, we consider T_{exo} = 180K.

5.2 Sensitivity to the density profiles in the lower thermosphere.

We have performed the same derivation using the hydrogen and deuterium density profiles given by case 2: constant hydrogen and deuterium densities between 80 and 120 km (see section 3) for the full set of observations during the period 3. The results are summarized in Table 4.

case

Because the hydrogen Lyman-α emission is optically thick, a large change of hydrogen density leads to a small variation in brightness. Therefore, the derived atomic hydrogen density is very sensitive to the absolute calibration of a UV spectrograph and we expect the derived D/H ratio to be also very sensitive to the calibration. The uncertainty on the solar flux at the center of the Lyman-α has the same effect because the simulated brightness is proportional to it.

To check the sensitivity of the derived densities and D/H, we consider an uncertainty of 20% in the absolute calibration and multiply the observed brightness by a factor A = 0.8 or 1.2. Such uncertainty is near the absolute calibration uncertainty as estimated by Chaffin et al. (2018). The derived parameters are summarized in Table 5.

A nH (80)

increase of both D and H densities, the derived D/H ratio is less sensitive to the absolute calibration. The uncertainty on the derived D/H ratio associated to an uncertainty of 20% on the absolute calibration can be at most a factor of 10 and less than 2 for an uncertainty of 10% on the absolute calibration (or solar flux at Lyman-α). Fits of Lyman-α profiles, including a scaling factor "1/A" on the modeled brightness as a free parameter, suggest a value of ~ 0.9 is most likely (Chaffin et al. 2018). This is equivalent to multiplying the observed brightness by A=1.1, which indicates that case A=0.8 is unlikely. If we don't consider this case, the uncertainty on the D/H ratio is reduced to a factor of 2.5.

5.4) Sensitivity to the estimate of the interplanetary medium brightness

We also perform a sensitivity study with the estimated brightness of the interplanetary medium, the derived parameters are less sensitive to it than the other parameters (Table 4). For this study we used a range of interplanetary hydrogen brightness (IPB) values expected at Mars (e.g. Chaufray et al. 2008).

IPB (kR)	nH (80)

All these factors are expected to be independent, the interplanetary medium brightness and IUVS calibration are obviously independent of the Martian atmosphere and one another, while the exospheric temperature is controlled by the EUV/FUV solar flux and the shape of the profile below 120 km is controlled by the water vapor in the mesosphere. Their combined effects on the retrieved parameters however are not independent. For example, using a scale factor A=1.2 will reduce the sensitivity to the interplantery brightness since its relative brightness will decrease. Therefore, the overall systematic uncertainty is not straightforward to derive but the analysis above indicates the most important effects.

6. Results and Discussion

6.1) Period 1: December 2016

We first estimate the D/H ratio from the two first periods where simultaneous limb observations were performed with the two spectral modes by IUVS. For period 1, using the empirical relationship between the solar Lyman-α flux (~ 3.3×10^{-3} W/m^2 for this period) and the dayside exospheric temperature from Bougher et al. (2017), leads to a temperature of 220K.

All the observations are performed close to the terminator in the winter hemisphere, i.e., close to regions unilluminated for an entire Martian season and partly heated by polar warming. The local exospheric temperature is expected to be lower than the dayside temperature. Global Martian Circulation Models and MAVEN/NGIMS observations suggest exospheric temperature ~ 120 - 140 K on the nightside (Gonzalez-Galindo et al. 2009, Bougher et al. 2015, Stone et al. 2018). We therefore consider an exospheric temperature T between 160 – 200 K. This choice is also justified a-posteriori because for temperatures larger than 200 K, the derived D brightness is larger than the D brightness measured with the high-resolutionmode (as shown in section 5.1). This choice is also

in agreement with the temperature at SZA=90° used by Mayyasi et al. (2019). The derived D/H ratio is very sensitive to this choice which is one of the main limiting aspects of the method as discussed in section 5.

The hydrogen and deuterium densities at the exobase are the free parameters used to fit the total Lyman-α brightness measured by IUVS. We perform such a fit for the 8 observations and 5 spatial bins (we excluded bin 0 and bin 6) of each observation independently. An example of the best fit of Lyman-α brightness for H, D and the sum is shown for T = 180K in Figure 8. The average values of the D and H brightness profiles measured with the high-resolutionmode (see section 2) are also shown. For clarity, we only display one limb scan, but similar results are obtained for other limb scans. Although, the deuterium brightness profile is closer to the deuterium average high-resolution mode profile for limb scan 1, and the hydrogen profile closer to the hydrogen average high-resolution mode profile for limb scan 4.

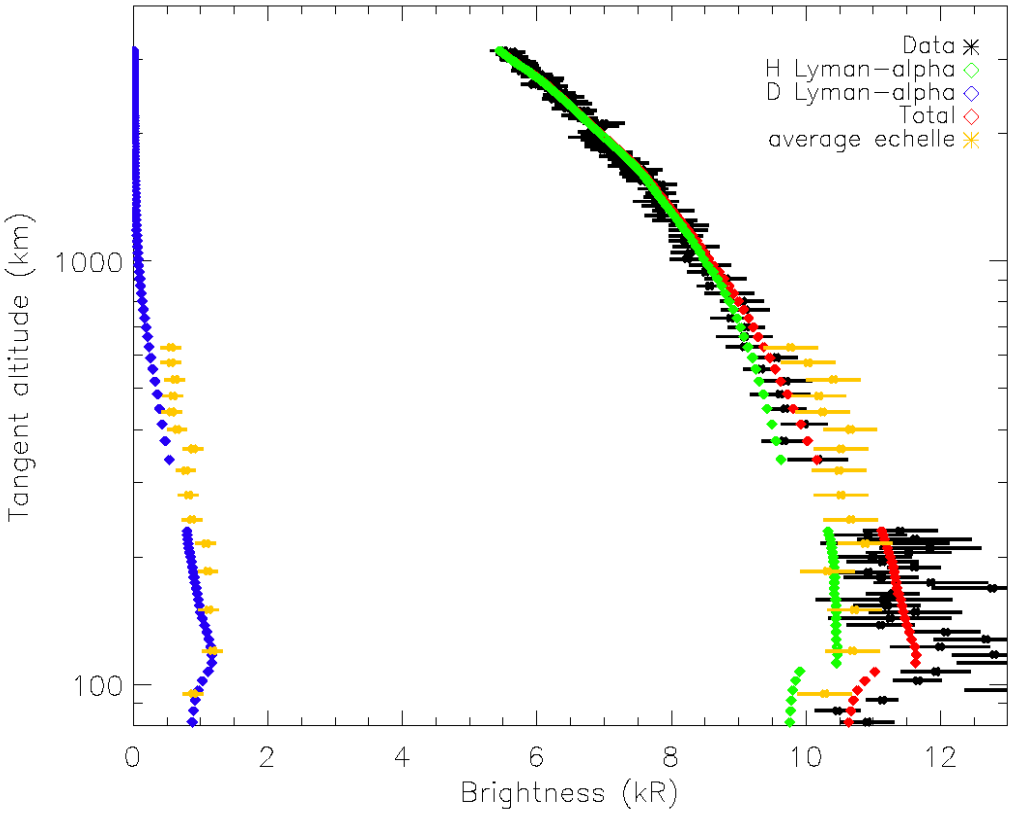

Figure 8. Vertical variations of the Lyman-α brightness observed by MAVEN/IUVS during orbit #4370 (using band 1) compared to the hydrogen and deuterium Lyman-α brightness and their sum derived from the best fit. For clarity, only one of the four limb scans is shown. The average deuterium and hydrogen Lyman-α profiles derived from the high-resolution mode are also indicated (orange stars) for information.

The different observations can be reproduced reasonably. Below 160 km, the observed brightness is slightly larger than the best-fit modeled brightness (see also Fig. 6). This difference could be due to emissions from proton aurorae, not included in the fit (Halekas et al. 2015, Deighan et al. 2018, Ritter et al. 2017; Hughes et al., 2019). The proton aurora brightness is sharply peaked near the bright limb with a scale height equal to the CO_2 density scale height (~ 10km), much less than the deuterium scale height (~ 100 km).

The estimated deuterium and hydrogen Lyman-α brightness are in reasonable agreement with the high-resolution mode average profile (Fig. 8). This confirms that during this season, part of the observed bright limb with the low-resolution mode is likely due to deuterium, as expected, and allows constraining the properties of the deuterium emission from the Lyman-α brightness profile near the limb, even if the D and H Lyman-α lines are not spectrally resolved. Above 1000 km, the contribution of the deuterium brightness to the total brightness is negligible. No large variations are derived from this set of observations. The deuterium density at the exobase is between 2.3-7.0x10^3 cm^{-3}, mostly larger than the deuterium density at the subsolar point derived by Mayyasi et al. (2019) from a large set of high-resolution observations (3000±1000 cm^{-3}). Such a difference can be attributed to local time variations, since an increase of the deuterium abundance from dayside to nightside is expected (Chaufray et al. 2015a). The derived deuterium and hydrogen densities at 80 km (below the homopause) for an exospheric temperature of 160, 180 and 200 K are given in Table 3. The derived D/H ratio at 80 km is between 1.3 – 3.6 x10^{-3}, which is larger than the D/H ratio measured in the water vapor (9±4x10^{-4}) near the surface of Mars (Owen et al. 1988). Other effects due to HDO and H_2O condensation and photochemistry (Bertaux and Montmessin 2001, Krasnopolsky 2002), and exospheric balistic transport (Chaufray et al. 2018), are not included in our simple models and should be included to better estimate the full vertical D/H profile. Assuming a constant D/H ratio below 120 km to roughly mimic the effect of photochemistry on the density profile would lead to an even larger derived D/H ratio at 80 km.

6.2) Period 2: September 2018

As for the previous period, simultaneous observations from low-resolution and high-resolution modes were performed during this period. Six “outlimb” scans were observed for each orbit, with tangent altitude moving from ~ 80 to 300 km with the low-resolution mode. During the same

period, four limb scans were performed with the high-resolution high-resolution mode. The SZA at the tangent point is different for each "outlimb" scan (Table 1). The expected dayside temperature derived from the empirical relation of Bougher et al. (2017) is 220 K. Best fits are obtained with an exospheric temperature of 180 K. An example of Lyman-α brightness for H, D and their sum, derived from the best fit, are shown for T = 180K in Figure 9. The average brightness profile of D and H, measured with the high-resolution mode (see section 2), is also shown for comparison in Figure 9. The derived deuterium and hydrogen brightnesses are in good agreement with the average profiles for the two species above 160 km.

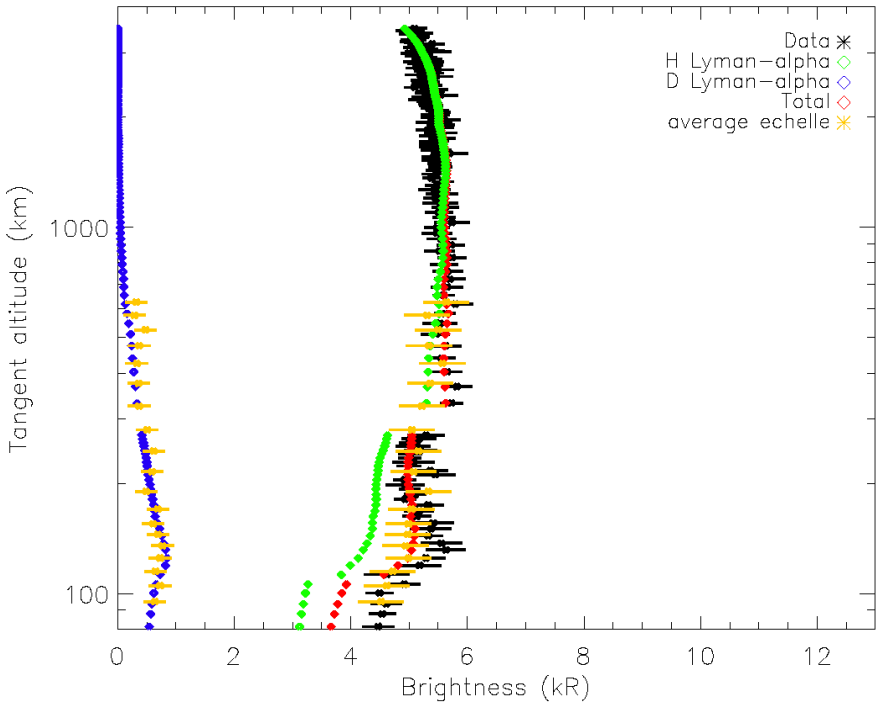

Figure 9. Vertical variations of the Lyman-α brightness observed by MAVEN/IUVS during orbit #7788 in spatial bin 1 compared to the hydrogen and deuterium Lyman-α brightness and their sum derived from the best fit. For clarity, we only show one of the four limb scans below 300 km. For this data SZA = 63° while the observations above 300 km were at SZA = 54° explaining the small discontinuity of the observed brightness near 300 km. The average deuterium and hydrogen Lyman-α profiles derived from the high-resolution mode (orange stars) are also shown for comparison.

The observed profile below 160 km, not used to derive the free parameters, is not well reproduced. A better fit would be obtained with a weak proton aurorae (few 100s R) during this period. Table 7 summarizes the derived parameters for exospheric temperatures between 180 – 220 K. Note that the derived D/H ratio is slightly less sensitive to the temperature inside this temperature range than at temperatures considered for the previous period (Table 2), and the derived D/H ratio decreases with the temperature.

T

This period corresponds to a season without deuterium detection in the high-resolution mode data (Mayyasi et al. 2017). The deuterium brightness is expected to be less than 300 Rayleighs, much lower than the hydrogen brightness, and therefore, we do not expect to characterize the deuterium emission in the low-resolution mode. We use this period of observations to check that our method correctly predicts no deuterium detection. These observations had SZA ~ 60° (Table 1) and thus the exospheric temperature can be estimated directly from the empirical relation between the solar flux and the temperature derived by Bougher et al. (2017), leadingto a temperature between 180 – 220 K. Contrary to periods 1 and 2, for this period we consider the density profile case 2 because no water vapor is expected to reach the lower thermosphere and therefore the density profiles should be controlled by the photochemical reactions between H_2 and ions (Krasnopolsky 2002, 2019). For most of the observed profiles, the best fit is obtained without deuterium, for example as shown in Figure 10.

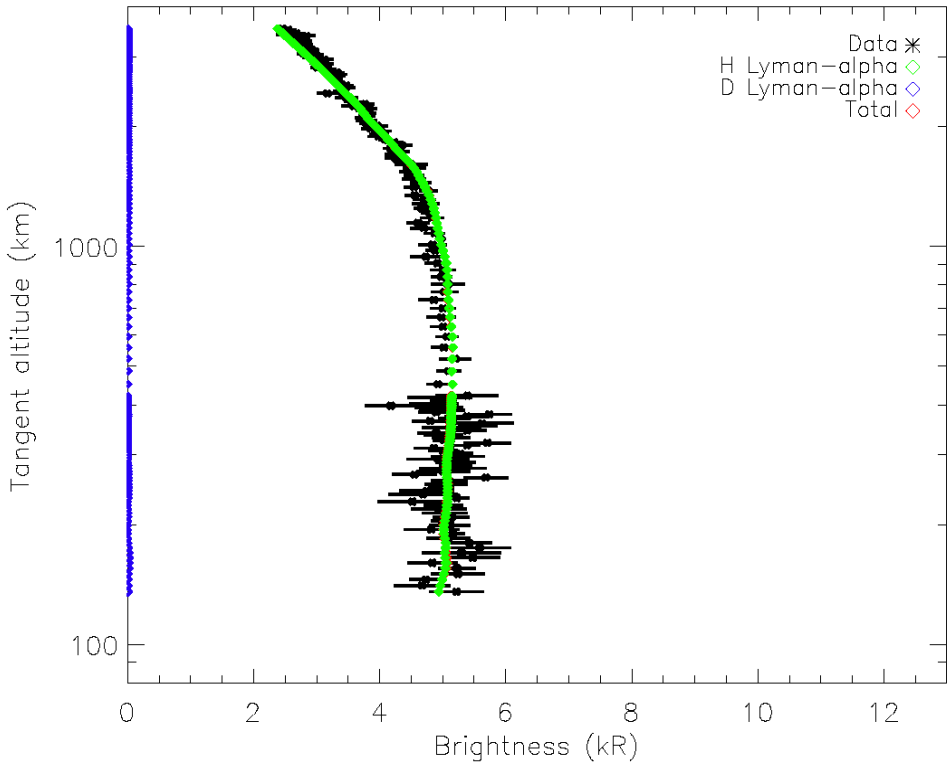

Figure 10. Vertical variations of the Lyman-α brightness observed by MAVEN/IUVS during orbit #1570 on spatial bin 1 compared to the hydrogen and deuterium Lyman-α brightness and their sum derived from the best fit, assuming an exospheric temperature of 200K.

This result agrees with the absence of a strong deuterium signal (larger than 300 R) directly measured with the high-resolution mode. The derived hydrogen density at 200 km is between 0.8 – 1.5 x 10^5 cm^{-3} depending on the exospheric temperature. Assuming a D/H ratio of 1x10^{-3} at 200 km, close to the value measured in the lower atmosphere, we should expect a deuterium density of ~ 80 – 150 cm^{-3} at 200 km, which gives us a lower limit estimate of the deuterium density at 200 km detectable by our method. Using case 1 profiles does not change the results, in that case, the best fit is also obtained without deuterium and the derived hydrogen density at 200 km is between 0.8 – 1.4 x 10^5 cm^{-3}. This density is lower than the density derived from the other periods near

southern summer, as expected from the seasonal variations of the hydrogen density (Chaffin et al. 2014, Bhattacharyya et al. 2017, Chaufray et al. 2021).

6.4) Period 4: Feb – March 2015

The observations for this period were made at the morning terminator near 30°S latitude (see Table 1), and, like periods 1 and 2, were near perihelion. At this time, the solar flux at Lyman-α (and therefore the exobase temperature) was larger than the December 2016 or the September 2018 period by ~ 20% (Table 1), and rescaling the temperature used for December 2016 by 20% would lead to a temperature ~260 K. However, these observations were performed near the morning terminator where the horizontal temperature gradient is large and the temperature lower than other parts of the terminator (Stone et al. 2018). Therefore, for this period, we will consider an exobase temperature between 180 and 220 K. The sensitivity of the derived D/H ratio with the assumed exospheric temperature is given in Table 8. The fits are slightly better for T =180 K while for temperatures larger than 200 K, the deuterium brightness reached 2 kR which is rather large compared to what has been observed with the high-resolution mode thus far (e.g. Mayyasi et al. 2019). As indicated in Table 8, the derived D/H ratio at 80 km is closer to the value measured in the lower atmosphere when assuming T = 180 K.

T

confirming that these profiles, which could not be fit with a singlehydrogen population for these observations (Chaffin et al. 2015), can be fit by including the non-negligible D Lyman-α emission. As shown in Fig. 11, the brightness profile is also well reproduced below 160 km, suggesting that proton aurorae were negligible during this period. Includingthe profile below 160 km in the fit doesnot change the derived average deuterium and hydrogen densities for this period.

Figure 11. Vertical variations of the Lyman-α brightness observed by MAVEN/IUVS during orbit #786 on band 1 compared to the hydrogen and deuterium Lyman-α brightness and their sum derived from the best fit, assuming an exospheric temperature of 180K.

Chaffin et al. (2018) studied a set of profiles performed with the low-resolution mode in December 2014 (Ls = 250-260°), at latitude 50° S and local time 3 pm, slightly before these observations. Only the Lyman-α brightness profile above 500 km was fitted for three different assumptions: only

a thermal hydrogen population, hydrogen and deuterium, and a thermal and non-thermal hydrogen population. For the second assumption, the derived average hydrogen density at 200 km was equal to 1.2×10^6 cm^{-3}, the average exospheric temperature 190 K, and the average deuterium density at 200 km equal to 4700 cm^{-3}, resulting in a derived D/H ratio of ~ 4×10^{-3}. The hydrogen and deuterium densities are slightly lower than those we derive for period 4, but are consistent with an increase of light species abundances near morning terminator. However, this comparison should be considered carefully since a scale parameter A = 0.87 was also derived from the fits, which would further reduce the derived densities (see section 5).

As for period 1, the derived deuterium density at 200 km (between 4-9×10^3 cm^{-3}) for the period 4 data is larger than the derived density at the sub-solar point from high-resolution observations (Mayyasi et al. 2019), which can be explained due to a larger deuterium density at the terminator than the sub-solar point, especially at morning side (Chaufray et al. 2015, 2018). The ranges of the derived hydrogen and deuterium densities at 80 km (below the homopause) for the full set of observations are given in Table 8. The derived range of D/H at 80 km is between [0.6 – 3.7] x 10^{-3} respectively, lower than the derived D/H ratio during period 1, but in the range of the D/H ratio measured during period 2 and in Martian water vapor. The derived hydrogen density at 200 km, between 0.6 – 4.5 $\times 10^6$ cm^{-3}, is larger than the simulated hydrogen density (Chaufray et al. 2018) whichcould be attributed to a larger amount of wator vapor at high altitudes during this season (Chaufray et al. 2021).

7. Conclusion

In this paper, we present the first detailed estimates of the D/H ratio deduced from total Lyman-α vertical profiles observed with the low-resolution mode of MAVEN/IUVS for four different

periods. The D/H ratio can be derived from low-resolution data during the southern summer period, when the deuterium emission is at its brightest and represents ~ 10% of the hydrogen emission below 300 km. Most of the uncertainty in the derived densities and D/H ratio are not due to noise in the databut rather caused by assumptions made in the models to derive the D/H ratio, and the absolute calibration. Specifically, 1) the exospheric temperature, 2) the density profile below 120 km and 3) absolute calibration used for the retrieval, can lead to systematic error in D/H at 80 km of a factor of ~ 10. This is currently the main limitation of our method however the two first assumptions could be improved in the future, (e.g., by using improved2D or 3D empirical/numerical temperature model distributions for different seasons, as done by Bhattacharyya et al. 2020). For the first two periods studied, near simultaneous observations were performed with the IUVS high-resolution mode and low-resolution mode making it possible to provide an estimate of the exospheric temperatures based on the best fit. For the third period, when the deuterium abundance is expected to be very low in the upper atmosphere, no deuterium is detected usingour method. For the fourth period, the presence of deuterium can explain the shape of the vertical brightness profiles and be used to estimate the D/H ratio even though no high-resolution mode observations were performed. Although the systematic errors due to the retrieval method are rather large, these may be improved upon in the future. This method could be useful for estimating the D/H ratio in the upper atmosphere of Mars on future missions lacking high-spectral resolution UV channels, such as for the Emirates Mars Mission launched in 2020.

Acknowledgements

This work and the MAVEN project are supported by NASA through the Mars Exploration Program. All IUVS outbound limb (“outlimb”) data used in this paper with revision/version tag v13_r01 are archived in NASA’s Planetary Data System:

http://atmos.nmsu.edu/data_and_services/atmospheres_data/MAVEN/maven_iuvs.html. We thank Ben Johnston for a careful read of the paper. J-Y. Chaufray is supported by the Centre National d'Etudes Spatiales. The simulated hydrogen and deuterium densities used in this paper are archived in https://owncloud.latmos.ipsl.fr/index.php/s/RtXhJBc8EwyLnrI and on Zenodo, doi: http://doi.org/10.5281/zenodo.4597518.

References

Bertaux, J.-L., J.T. Clarke, M. Mumma, T. Owen, and E. Quemerais (1992), A Search for the Deuterium Lyman-alpha Emission from the Atmosphere of Mars, in Science with the Hubble Space Telescope, ESO Proc. No. 44, 459

Bertaux, J-L. and F. Montmessin, (2001), Isotopic fractionation through water vapor condensation: The deuteropause, a cold trap for deuterium in the atmosphere of Mars, J. Geophys. Res., 106, E12, 32,879-32,884

Bhattacharyya, D., J.T. Clarke, J-L. Bertaux, J-Y. Chaufray, and M. Mayyasi, (2017) Analysis and modeling of remote observations of the martian hydrogen exosphere, Icarus, 281, 264-280

Bhattacharyya, D., J. Y. Chaufray, M. Mayyasi, J. T. Clarke, S. Stone, R. V. Yelle, W. Pryor, J. L. Bertaux, J. Deighan, S. K. Jain, and N. M Schneider (2020), Two-dimensional model for the martian exosphere: Applications to hydrogen and deuterium Lyman alpha observations, Icarus, doi: 10.1016/j.icarus.2019.113573.

Bougher, S.W., D. Pawlowski, J.M. Bell, S. Nelli, T. McDunn, J.R. Murphy, M. Chizek, and A. Ridley, (2015), Mars Global Ionopshere-Thermosphere Model (MGITM): Solar cycle, seasonal and diurnal variations of the Mars upper atmosphere, J. Geophys. Res. Planets., 120, 311-342

Bougher, S.W., K.J. Roeten, K. Olsen, P.R. Mahaffy, M. Benna, M. Elrod, S.K. Jain, N.M.

Schneider, J. Deighan, E. Thiemann, F.G. Eparvier, A. Stiepen, and B. Jakosky, (2017), The structure and variability of Mars dayside thermosphere from MAVEN NGIMS and IUVS measurements : Seasonal and solar activity trends in scale heights and temperatures, J. Geophys. Res. Space Phys., 122, 1296-1313

Cangi, E., M. Chaffin, and J. Deighan, Higher martian atmospheric temperatures lead to enhanced D/H fractionation and water loss, arXiv:2007.12589, (2020)

Chaffin, M., J-Y. Chaufray, J. Deighan, N.M. Schneider, W.E. McClintock, A.I.F. Stewart, E. Thiemann, J.T. Clarke, G.M. Holsclaw, S.K. Jain, M.M.J. Crismani, A. Stiepen, F. Montmessin, F.G. Eparvier, P.C. Chamberlain, and B.M. Jakosky, (2015), Three-dimensional structure in the Mars H corona revealed by IUVS on MAVEN, Geophys. Res. Lett., 42, 9001-9008, doi: 10.1002/2015GL065287

Chaffin, M.S., J. Deighan, N.M. Schneider, and A.I.F. Stewart, (2017), Elevated atmospheric escape of atomic hydrogen from Mars induced by high-altitude water, Nat. Geosc., 10, 174-178

Chaffin, M.S., J-Y. Chaufray, J. Deighan, N.M. Schneider, M. Mayyasi, J.T. Clarke, E. Thiemann, S.K. Jain, M.M.J. Crismani, A. Stiepen, F.G. Eparvier, W.E. McClintock, A.I.F. Stewart, G.M. Holsclaw, F. Montmessin, and B. Jakosky, (2018), Mars H escape rates derived from MAVEN/IUVS Lyman-α brightness measurements and their dependence on model assumptions, J. Geophys. Res : Planets, 123, 2192-2210

Chamberlain, J.W., (1963), Planetary coronae and atmospheric evaporation, Planet. Space Sci., 11, 901-960

Chamberlain, J.W., and G.R. Smith, (1971), Comments on the rate of evaporation of a non-maxwellian atmosphere, Planet. Space Sci., 19, 675-684

Chaufray, J-Y., J-L. Bertaux, F. Leblanc, and E. Quémerais, (2008), Observation of the hydrogen corona with SPICAM on Mars Express, Icarus, 195, 598-613

Chaufray, J-Y., J-L. Bertaux, E. Quémerais, E. Villard, F. Leblanc, Hydrogen density in the dayside venusian exosphere derived from Lyman-α observations by SPICAV on Venus Express, Icarus, 217, 767-778, 2012

Chaufray, J-Y., F. Gonzalez-Galindo, F. Forget, M.A. Lopez-Valverde, F. Leblanc, R. Modolo, and S. Hess, (2015a), Variability of the hydrogen in the martian upper atmosphere as simulated by a 3D atmosphere-exosphere coupling, Icarus, 245, 282-294

Chaufray, J-Y., J-L. Bertaux, F. Leblanc, E. Quémerais, and S. Sulis, (2015b), Observations of the nightside venusian hydrogen corona with SPICAV/VEX, Icarus, 262, 1-8

Chaufray, J-Y., R.V. Yelle, F. Gonzalez-Galindo, F. Forget, M. Lopez-Valverde, F. Leblanc, R. Modolo, (2018), Effect of the lateral exospheric transport on the horizontal hydrogen distribution at the exobase of Mars, J. Geophys. Res., 123, 4241-4254, doi : 10.1002/2017JA025163

Chaufray, J-Y., M. Chaffin, J. Deighan, S. Jain, N. Schneider, M. Mayyasi, and B. Jakosky, Effect of the 2018 Martian global dust storm on the CO2 density in the lower nightside thermosphere observed from MAVEN/IUVS Lyman-alpha absorption, Geophys. Res. Lett., 47, e2019GL082889, (2020)

Chaufray, J-Y., F. Gonzalez-Galindo, M.A. Lopez-Valverde, F. Forget, E. Quémerais, J-L. Bertaux, F. Montmessin, M. Chaffin, N. Schneider, J.T. Clarke, F. Leblanc, R. Modolo, and R. Yelle, (2021), Study of the hydrogen escape rate at Mars during Martian years 28

and 29 from comparisons between SPICAM/Mars Express observations and GCM-LMD simulations, Icarus, (in press), doi : 10.1016/j.icarus.2019.113498.

Clarke, J.T., M. Mayyasi, D. Bhattacharyya, N.M. Schneider, W.E. McClintock, J.I. Deighan, A.I.F. Stewart, J-Y. Chaufray, M.S. Chaffin, S.K. Jain, A. Stiepen, M. Crismani, G.M. Holsclaw, F. Montmessin, and B. Jakosky (2017), Variability of D and H in the Martian upper atmosphere observed with the MAVEN IUVS echelle channel, J. Geophys. Res., 122, 2336-2344, doi: 10.1002/2016JA023479

Deighan, J., M.S. Chaffin, J-Y. Chaufray, A.I.F. Stewart, N.M. Schneider, S.K. Jain, A. Stiepen, M. Crismani, W.E. McClintock, J.T. Clarke, G.M. Holsclaw, F. Montmessin, F.G. Eparvier, E.M.B. Thiemann, P.C. Chamberlin, and B.M. Jakosky, MAVEN IUVS observation of the hot oxygen corona at Mars, Geophys. Res. Lett., 42, 9009-9014, doi:10.1002/2015GL065487, (2015)

Deighan, J., S.K. Jain, M.S. Chaffin, X. Fang, J.S. Halekas, J.T. Clarke, N.M. Schneider, A.I.F. Stewart, J-Y. Chaufray, J.S. Evans, M.H. Stevens, M. Mayyasi, A. Stiepen, M. Crismani, W.E. McClintock, G.M. Holsclaw, D.Y. Lo, F. Montmessin, F. Lefèvre, and B. Jakosky, (2018), Discovery of a proton aurora at Mars, Nature Astron., 2, 802-807

Elrod, M.K., S. Bougher, J. Bell, P.R. Mahaffy, M. Benna, S. Stone, R. Yelle, and B. Jakosky, (2017), He bulge revealed: He and CO2 diurnal and seasonal variations in the upper atmosphere of Mars as detected by MAVEN NGIMS, J. Geophys. Res. Space Physics, 122, 2564-2573, doi: 10.1002/2016JA023482

Emerich, C., P. Lemaire, J-C. Vial, W. Curdt, U. Schüle, K. Wilhelm, (2005), A new relation between the central spectral solar H I Lyman α irradiance and the line irradiance measured by SUMER/SOHO during the cycle 23., Icarus, 178, 429-433

Encrenaz, T., C. DeWitt, M.J. Richter, T.K. Greathouse, T. Fouchet, F. Montmessin, F. Lefèvre, B. Bézard, S.K. Atreya, S. Aoki, and H. Sagawa, New measurements of D/H on Mars using EXES aboard SOFIA, A&A, 612, A112, (2018)

Gerard, J-C., B. Hubert, B. Ritter, V.I. Shematovich, and D.V. Bisikalo, Lyman-α emission in the Martian proton aurora: line profile and role of horizontal induced magnetic field., Icarus, 321, 266-271, (2019)

Gonzalez-Galindo, F., F. Forget, M.A. Lopez-Valverde, M. Angelats i Coll, and E. Millour, A ground-to-exosphere Martian general circulation model: 1 Seasonal, diurnal, and solar cycle variation of thermospheric temperatures, J. Geophys. Res., 114, E04001, doi:10.1029/2008JE003246, 2009

Gonzalez-Galindo, F., M.A. Lopez-Valverde, F. Forget, M. Garcia-Comas, E. Millour, and L. Montabone, (2015), Variability of the Martian thermosphere during eight Martian years as simulated by a ground-to-exosphere global circulation model, J. Geophys. Res., 120, 2020-2035, doi:10.1002/2015JE004925

Halekas, J.S., R.J. Lillis, D. L. Mitchell, T.E. Cravens, C. Mazelle, J.E.P. Connerney, J.R. Espley, P.R. Mahaffy, M. Benna, B.M. Jakosky, J.G. Luhmann, J.P. McFadden, D.E. Larson, Y. Harada, and S. Ruhunusiri, (2015), MAVEN observations of solar wind hydrogen deposition in the atmosphere of Mars, Geophys. Res. Lett., 42, 8901-8909

Hughes A., M. Chaffin, E. Mierkiewicz, J. Deighan, S. Jain, N. Schneider, M. Mayyasi, and B. Jakosky (2019), Proton aurora on Mars: A dayside phenomenon pervasive in southern summer, J. Geophys. Res., doi: 10.1029/2019JA027140.

Krasnopolsky, V., M.J. Mumma, and G.R. Gladstone, (1998), Detection of atomic deuterium in the upper atmosphere of Mars, Science, 280, 1576, doi: 10.1126/science.280.5369.1576

Krasnopolsky, V., Mars' upper atmosphere and ionosphere at low, medium, and high solar

activities: Implications for evolution of water, J. Geophys. Res., 107(E12), 5128, doi: 10.1029/2001JE001809, 2002

Krasnopolsky, V., Photochemistry of water in the martian thermosphere and its effect on hydrogen escape, Icarus, 321, 62-70, (2019)

Mayyasi, M., J.T. Clarke, D. Bhattacharyya, J. Deighan, S. Jain, M. Chaffin, E. Thiemann, N. Schneider, and B. Jakosky, (2017), The variability of atmospheric deuterium brightness at Mars: Evidence for seasonal dependence, J. Geophys. Res.: Space Phys., 122, 10,811-10,823

Mayyasi, M., J. Clarke, D. Bhattacharyya, J-Y. Chaufray, M. Benna, P. Mahaffy, S. Stone, R. Yelle, E. Thiemann, M. Chaffin, J. Deighan, S. Jain, N. Schneider, and B. Jakosky, (2019), Seasonal variability of deuterium in the upper atmosphere of Mars, J. Geophys. Res: Space Physics., 124, 2152-2164

McClintock, W.E., N.M. Schneider, G.M. Holsclaw, J.T. Clarke, A.C. Hsokins, I. Stewart, F. Montmessin, R. Yelle, and J. Deighan (2015), The Imaging ultraviolet spectrograph (IUVS) for the MAVEN Mission, Space Sci. Rev., doi:10.1007/s11214-014-0098-7

Owen, T., J-P. Maillard, C. De Bergh, and B.L. Lutz, (1988), Deuterium on Mars : The abundance of HDO and the D/H value, Science, 240, 1767-1770

Ritter, B., J-C. Gerard, B. Hubert, L. Rodriguez, and F. Montmessin, (2017), Observations of the proton aurora on Mars with SPICAM on board Mars Express, Geophys. Res. Lett., 45, https://doi.org/10.1002/2017GL076235

Stone, S., Yelle, R., Benna, M., Elrod, M., & Mahaffy, P. (2018). Thermal structure of the Martian upper atmosphere form MAVEN NGIMS, Journal of Geophysical Research: Planets, 123, 2842–2867. https://doi.org/10.1029/2018JE005559

Vandaele, A-C., O. Korablev, et al., Martian dust storm impact on atmospheric H2O and D/H observed by ExoMars Trace Gas Orbiter, Nature, 568, 521-525, (2019)